Hosseini *et al. EURASIP Journal on Advances in Signal Processing* (2016) 2016:60
DOI 10.1186/s13634-016-0352-0

EURASIP Journal on Advances in Signal Processing

RESEARCH Open Access

Robust detection in ultra-wideband impulse radar using DPSS-MMSE estimator

S. M. Ali Tayaranian Hosseini[1], Hamidreza Amindavar[1*] and James A. Ritcey[2]

Abstract

In this paper, it has been shown that non-stationary received signals at ultra-wideband impulse radars can be addressed by Fourier series model with time-varying coefficients. Next, simply by computing statistical features of the coefficients, we show that this model can be considered as a sum of band-limited sources. Based on the unconditional orthonormal representation of band-limited signals, a MMSE estimator is introduced to determine the Fourier coefficients. Getting the most out of our novel estimator, we suggest a new method for blind and robust detection that enables us to determine the range and velocity of moving targets, accurately without utilizing any matched filters. In this new approach, no prior information is required for detection, except pulse repetition interval. Since the novel method is based on the non-stationary analysis, the signal is analyzed in a long period of time to estimate the velocity in high resolution. Furthermore, since there is no assumption on the noise distribution, the signal of interest can be simply detected in the presence of correlated and non-Gaussian noise, i.e., encompassing the conglomerate effects of clutter and interference. To verify our result, an experimental test and simulations are also presented comparing the new detector with conventional ultra-wideband impulse radar detectors referred to as interleaved periodic correlation processing (IPCP) in the literature.

Keywords: Robust detection, Ultra-wideband impulse, MMSE estimator

1 Introduction

The vast majority of traditional radars use harmonic pulse signals to detect targets. The bandwidth of signals used in such radars is much less than the carrier frequency. Consequently, these radars can provide only low resolution detection. However, in today's applications, high-resolution radars are sought for fine and sensitive surveillance of the environment.

Improving detected target range measurement accuracy, identifying target classes and types, low-altitude detection, ground penetrating, immunity to passive interference, and some other advantages have been provided by reducing the pulse width of signals in ultra-short pulse or ultra-wideband (UWB) impulse radars [1]. This type of the UWB radars, as a high-resolution radar, is widely used for remote sensing of the objects in medicine, psychophysiology [2], human being detection [3], through the wall imaging [4], and stealth target detection [1].

In some applications of ranging and velocity detection traditional correlation is used to increase signal-to-noise ratio [3]. Some factors such as multiple scattering points and dispersion make echo waveforms seriously distorted in ultra-short pulse radars; hence, the backscattered signal from a target upon impingement of an ultra-short pulse signal has a complex shape in time domain and is completely different from the transmitted waveform [5]. In addition, the radar cross section (RCS) in UWB target detection becomes time-dependent, so the concept of instantaneous target RCS has been introduced [6]. In such cases, the target scattered signal is non-stationary in time. These phenomena cause the traditional correlation detection method, which selects the transmitted signal as the reference waveform in the correlator, to degrade in detecting targets. The parameters such as duration, location, and amplitude of the scattered signal are strongly dependent on the target geometry. Since the scattered signal from a target is represented as a stochastic time series, hence, generally speaking, its mathematical description is unknown. Therefore, blind detection has attracted the attention of advanced ultra-short pulse radar designers.

*Correspondence: hamidami@aut.ac.ir
[1] Amirkabir University of Technology, Tehran, Iran
Full list of author information is available at the end of the article

A blind detector based on the correlation of the received signals in two adjacent periods, has been introduced as the interleaved periodic correlation processing (IPCP) detector [7]. In the IPCP, an invariable channel in at least two adjacent periods is assumed. The first period is considered as the reference signal and matched filter for the second one. Because the reference signal may be completely different from a real reference (transmitted signal), this approach causes noticeable degradation in detection compared to the optimum matched filter in complicated scenarios such as moving target scenarios. In the aforementioned detector, the integration period of the correlation processing is determined by the observation interval or the scattered signal duration which depends on the target size. Hence, the detection threshold is unknown and depends on the target size [8]. Another prominent issue, which we will show in this article, is that the mentioned correlation processing, IPCP, causes removal of the Doppler information, a major drawback in determining the velocity of a moving target accurately. Another approach is introduced in [9], used in human being detection; there is no correlation processing and detection is based on the frequency characteristics of the wideband backscattered signals. In this application, Doppler shift is negligible, and generally speaking, velocity estimation is not important. Although the Doppler shift is really small, extraction of Doppler shift is the base of the some nowadays strategies in this application [10, 11]. The velocity measurements in ultra-short pulse radar is considered in [6, 12] by taking the advantage of the conventional correlation detectors. However, these measurements are also limited in the resolution of velocity estimation. Due to these limitations, velocity, which can be used as an important parameter in the tracking filters in applications such as UWB radar sensor networks, has often been ignored [13]. In another procedure, a UWB detection radar is introduced based on cell averaging constant false alarm rate (CA-CFAR)[14]. CA-CFAR is a powerful technique that reduces the false alarm rate in a given probability of detection, especially in the presence of clutter and jamming signals. However, it is not consider the non-stationarity issues in the interest signal and clutter. Therefore, extraction of velocity is not possible by only CA-CFAR technique.

There are some limitations to produce short time pulses [6]. Since the Fourier series method for waveform generation overcomes these limitations [15], UWB radar signals are generated using the Fourier series-based waveform paradigm [15]. The present article is based on the Fourier series signal generation. Here, it is shown that the UWB received signal is an almost periodic signal which can be represented as a Fourier series expansion with time-varying coefficients. Cyclostationary characteristics which appear in this type of waveform can be exploited to determine a blind detector which is based on detecting the presence of cyclostationarity. Cyclostationary detection is examined in [16]. Although cyclostationary features appear in these kind of signals, actually, there is no pure cyclostationarity, especially, when the observations have to be made in large intervals and high resolution, velocity estimation is intended. In this article, in Section 2, we first describe the model of received ultra-short pulse signal scattered from a target, based on Fourier series model for transmitted signal. Then, in Section 3, we will do an analysis on the IPCP detector and demonstrate its inability in velocity detection. Next, we aim to show that the non-stationary received signal can be modeled by a Fourier series with time-varying coefficients. In Section 4, we have used here time-varying orthonormal sequences as the optimal weights, that is an index-limited sequence with maximum energy concentration in a finite sample interval to introduce a linear MMSE estimation for the time-varying coefficients. The aforementioned optimal window is related to the discrete prolate spheroidal sequences (DPSS) [17]. In Sections 5 and 6, based on the estimation of the coefficients, we extract range and velocity of targets. We fully describe the analysis of resolution of range and velocity and the error estimation. Because of utilization of time-varying weights in the estimation of range and doppler, which leads to the estimation of non-stationary signals, the novel estimator is robust for a wide variety of lifelike scenarios including slow-moving or hovering platforms. Since there is no assumption on noise distribution, all analyses are done based on general correlated non-Gaussian noise. Therefore, the noise considered herein accounts for all interferences, clutters, and thermal noise. In Section 7, in simulations, using this signal, we have sketched the range-velocity plot to visualize the results of detection and ROC plot to verify the advantages of our work compared to IPCP. This will be done for both cases of Gaussian and non-Gaussian noise, as well as colored and white noise.

2 System model and problem formulation

In UWB radars, anomalies caused by the array antenna, the propagation path and scattering from the target, will change shape and bandwidth of the transmitted signal. In this section, the model of transmitted signal and the factors that may cause variations in the shape of a UWB signal during the radar observation of a target is discussed.

2.1 Fourier series model in ultra-short pulse

Most of the UWB radar waveforms considered in the literature are of the form of impulse signals which could be implemented by Marx-Bank or similar techniques [18]. In pulse generation, the energy stored in a long period of time have to be released in a short while. In Marx-Bank, as a typical way of energy storage, the capacitive

stored energy is released by switches such as spark gap, diode, and laser-actuated semiconductors which cause the pulse shape, and PRI is not precisely controllable [1]. The Fourier method of waveform generation [15] (combination of conventional heterodyning method in [1]) is an appropriate method to overcome these problems [1, 15]. In this method, the transmitted signal $s_1(t)$ is produced by the summation of a truncated Fourier series components.

The number of transmitting sources required to generate a short pulse train is a function of pulse width and duration. In this case, the pulse train $s_1(t)$ can be represented by a series of $N+1$ Fourier components as

$$s_1(t) = \sum_{n=-N/2}^{N/2} c_n e^{j\omega_n t}, \tag{1}$$

where $\omega_n = \frac{2\pi n}{\mathcal{T}}$, $\mathcal{T}$ is the total pulse duration of the signal and c_n are the complex harmonic coefficients. $s_1(t)$ assumed the transmitted baseband signal to be serve as an ultra-short pulse signal. For example the complex coefficients for the 11-chip Barker sequence with chip width of τ and pulse duration $\mathcal{T} = 11\tau$, can be written as

$$\begin{aligned} c_n = \frac{1}{\pi n}\frac{1}{2j}\left(1 - 2e^{-j\omega_n 3\tau} + 2e^{-j\omega_n 6\tau} - 2e^{-j\omega_n 7\tau}\right. \\ \left. + 2e^{-j\omega_n 9\tau} - 2e^{-j\omega_n 10\tau} + e^{-j\omega_n 11\tau}\right). \end{aligned} \tag{2}$$

It should be noted that after transmitting $s_1(t)$, there will be no other transmissions during the pulse repetition interval (PRI). So, the duration of the transmitted signal, comprising both the transmitted pulse $s_1(t)$ and zero, is PRI . As an example, the 11-chip Barker code is depicted in Fig. 1.

2.2 Effect of array antenna

We assume the UWB signal $s_1^c(t) = \mathrm{Re}\left\{s_1(t)\, e^{j2\pi f_c t}\right\}$ to be transmitted with the carrier frequency f_c in a form of current pulse by an array antenna with P radiators shown in Fig. 2. The effects of the array antenna change $s_1^c(t)$ to another pulse train $s_2^c(t)$. These effects, discussed in [7], are briefly explained in the following.

If the antenna radiators have a length of $L_r \gg c\tau$ (c is the velocity of light and τ is the pulse width), the antennae radiate several pulses of the electromagnetic wave serially. As a result, a single pulse transforms into a sequence of K pulses each of which radiates in a time interval ε_k. Another phenomenon occurs due to the spatial delay of radiated signals which is $(d_p/c)\cos(\phi)$, for adjacent radiators. Here d_p is the spacing between the radiators and ϕ is the observation angle of the radar. Therefore, the baseband signal $s_2(t)$ in the radiated waveform $s_2^c(t) = \mathrm{Re}\left\{s_2(t)\, e^{j2\pi f_c t}\right\}$ can be written as:

$$\begin{aligned} s_2(t) &= \sum_{p=1}^{P}\sum_{k=1}^{K} e^{j\phi_{kp}} s_1\left(t + \varepsilon_k + \frac{d_p}{c}\cos\phi\right) \\ \phi_{kp} &= 2\pi f_c\left(\varepsilon_k + \frac{d_p}{c}\cos\phi\right). \end{aligned} \tag{3}$$

If we assume uniform spacing between the radiators of distance d, Eq. (3) can be written as:

$$\begin{aligned} s_2(t) &= P\sum_{k=1}^{K} e^{j\phi_k} s_1\left(t + \varepsilon_k + \frac{d}{c}\cos\phi\right) \\ \phi_k &= 2\pi f_c\left(\varepsilon_k + \frac{d}{c}\cos\phi\right). \end{aligned} \tag{4}$$

2.3 Model of the target in UWB radar

Assume the maximum dimension of the target be L_t satisfying the condition $c\tau \ll L_t$. Then, the target can be modeled as a combination of M local scattering elements (bright point [8]). The delay of radiated signal $s_2^c(t)$ in arriving at the mth bright point is:

$$\tau_d^m = R(t)/c + \delta_m + \kappa_m(t), \tag{5}$$

where $R(t) = R - vt$, R is the distance from the receiver to the center of the target, v is the radial velocity of the target's combination, δ_m models the distance from the center of the target to the mth scatterer; and $\kappa_m(t)$ models time-varying aspect angle in the target's plate [19–22]. The signal $s_2^c(t)$ is reflected by the discrete target elements with various time delays τ_d^m and various attenuations α_m. The reflected signal will come back to the radar receiver

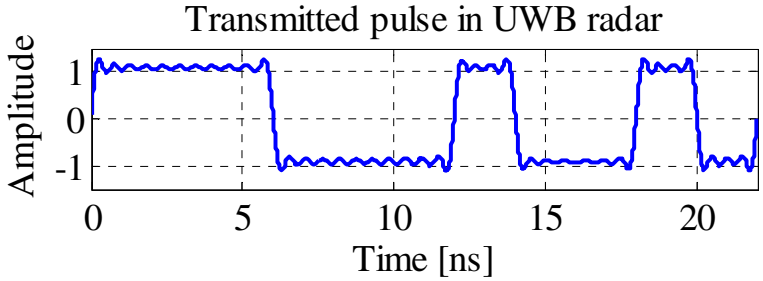

Fig. 1 A UWB pulse signal. This signal is generated by Fourier series model using 40 harmonies. The pulse is produced by the Barker code with the length of 11, chip width of 2 *ns* and the total pulse duration 22 of *ns*

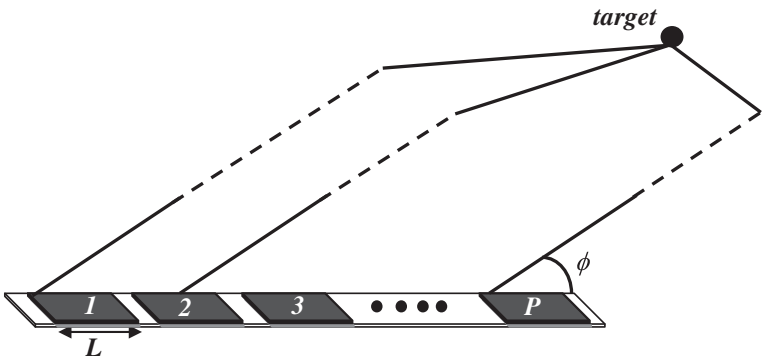

Fig. 2 Array antenna with *P* radiators

after τ_d^m. Hence, $s_3(t)$, the baseband received signal during one pulse repetition interval (T_{PRI}), is expressed as

$$s_3(t) = \sum_{m=1}^{M} \alpha_m e^{-j2\pi f_c(2\kappa_m(t))} e^{-j2\pi f_c(2\delta_m+2R/c)} e^{j2\pi F_d t} s_2(t-2\delta_m-2R/c). \quad (6)$$

In Eq. (6), because $v << c$, the vt/c and $\kappa_m(t)$, due to far field assumption, are very small and can be neglected in the argument of $s_2(t)$. α_m, the intensity of reflection of each bright point, has an statistical model based on the RCS models which is discussed in several literatures [8]. An ultra-short pulse signal possesses a large bandwidth that causes the radar cross section (RCS) to vary significantly. Therefore, in practical applications, the target RCS depends on the frequency [7]. The frequency-dependent RCS implies that α_m, previously assumed to be a single coefficient, should act as a FIR filter h_m with complex coefficients for each bright point. Hence, $s_3(t)$ is expressed as:

$$s_3(t) = \sum_{m=1}^{M} \int_0^{T_{PRI}} h_m(\xi-\delta_m-R/c) e^{j2\pi F_d \xi} s_2(\xi-t+2\delta_m+2R/c)\, d\xi. \quad (7)$$

Herein, instead of using $h_m(t)$ as a FIR filter, we utilize α_{mn} coefficients which depend on nth harmonic frequency. By substitution Eq. (1) in (4) and (4) in (6) and considering α_{mn} instead of α_m, the $s_3(t)$ during a pulse repetition interval can be represent as:

$$s_3(t) = \sum_{n=-N/2}^{N/2} a_n(t) e^{j\omega_n t} \quad (8)$$

$$a_n(t) = \sum_{m=1}^{M}\sum_{k=1}^{K} Pc_n \alpha_{mn} e^{-j2\pi f_c(2\kappa_m(t))} e^{j(\varphi_k+\phi_m+\theta_{nkm})} e^{j2\pi F_d t}$$

$$\varphi_m = 2\pi f_c(2\delta_m + 2R/c)$$

$$\theta_{nkm} = \omega_n\left(\varepsilon_k - 2\delta_m + \frac{d\cos(\phi)-2R}{c}\right).$$

Since the transmitted signal is repeated every T_{PRI}, we have $\omega_n = 2\pi n f_0$ where f_0 is the pulse repetition frequency. Equation (8) has been expressed for one T_{PRI}. This equation is valid in all time by assuming an almost periodic h_m with the period of pulse repetition interval which leads to uniform coefficients α_{mn} in every pulse repetition interval. This assumption for a finite number of pulse repetition intervals, will be reasonable if $2T_{CPI}v \ll c\tau$, where T_{CPI} is the time of coherent processing interval. The estimation of velocity for low speed targets (where v is small), needs the duration of coherent processing interval to be long enough. Therefore, in our scenario that the wide range of velocity detection is considered, α_{mn} cannot be assumed constant and varies smoothly in time. Equation (8) can be extended to be valid for every t if $a_n(t)$ is expressed as:

$$a_n(t) = \sum_{m=1}^{M}\sum_{k=1}^{K} Pc_n \alpha_{mn}(t) e^{-j2\pi f_c(2\kappa_m(t))} e^{j(\phi_k+\varphi_m+\theta_{nkm})} e^{j2\pi F_d t}. \quad (9)$$

In Appendix A, we find an expression for the correlation function and the spectrum of the time-varying coefficients $a_n(t)$. In there, we demonstrate that the $a_n(t)$ processes are band-limited signals all around the Doppler frequency. So, if a summation of N Fourier components is transmitted as an ultra-short pulse signal as mentioned before, the received signal will be a wideband signal composed of a sum of non-stationary signals each of which acts as a sine wave with a frequency nf_0, multiplied by a "smoothly varying" amplitude function. Therefore, the baseband received signal $s_3(t)$ is modeled as a Fourier series with time-varying coefficients $a_n(t)$. Based on what is described in this section, the scattering in UWB radar elongates the pulse width τ and changes the resolution of range gate. Because the number of pulses, time delay δ_m, and the intensity α_{mn} of the signal depends on the target shape and target element, we can use variation of

the pulse width as a feature in classification of targets. The scattered signal from a real target and its spectrum are depicted in Figs. 3 and 4, respectively. The experimental test to obtain the signal is discussed in Section 7. In next section, a linear MMSE estimation has been introduced to determine of the mentioned time-varying coefficients.

3 IPCP detector

Let $s(t)$ be the baseband transmitted signal, then, this signal is reflected back from a target with the velocity v at the range of R the received baseband signal is represented as

$$r(t) = e^{j2\pi F_d t}\widehat{s}\left(t - \frac{2R}{c}\right) + n(t), \tag{10}$$

where c is the speed of light, $F_d = \frac{2v}{\lambda}$ is the Doppler frequency, and λ is the wavelength of received signal. The effects of array antennas, anomalies due to the propagation path and effects of target scattering may change $s(t)$ to the pulse train $\widehat{s}(t)$, these effects will be discussed in Section 2. $n(t)$ is a zero mean additive noise which is independent of the transmitted signal.

The IPCP receiver uses the received signal as the reference signal. The receiver model is shown in Fig. 5. The output could be expressed as

$$U(nT_{PRI}) = \int_{nT_{PRI}}^{(n+1)T_{PRI}} r^*(\tau)\, r(\tau - T_{PRI})\, d\tau, \tag{11}$$

where T_{PRI} is the pulse repetition interval and n is the neutral number. Now, using Eq. (10) in Eq. (11), we have

$$U(nT_{PRI}) = e^{-j2\pi F_d T_{PRI}} \int_{nT_{PRI}}^{(n+1)T_{PRI}} \widehat{s}_3^*\left(\tau - \frac{2R}{c}\right)\widehat{s}\left(\tau - T_{PRI} - \frac{2R}{c}\right)d\tau \tag{12}$$

$$+ \int_{nT_{PRI}}^{(n+1)T_{PRI}} e^{-j2\pi F_d \tau}\widehat{s}^*\left(\tau - \frac{2R}{c}\right) n(\tau - T_{PRI})\, d\tau \tag{13}$$

$$+ \int_{nT_{PRI}}^{(n+1)T_{PRI}} e^{j2\pi F_d(\tau - T_{PRI})}\widehat{s}\left(\tau - T_{PRI} - \frac{2R}{c}\right)n^*(\tau)d\tau \tag{14}$$

$$+ \int_{nT_{PRI}}^{(n+1)T_{PRI}} n^*(\tau)\, n(\tau - T_{PRI})\, d\tau. \tag{15}$$

Since the noise and signal are uncorrelated, Eqs. (13) and (14) are zero. It can be seen in Eq. (12) that the Doppler frequency exists in a phase factor which is independent of the time sequence. Hence, velocity can not be extracted in the Doppler processing. Since the noise is zero mean and independent of the transmitted signal, there is no information about velocity in Eq. (13) or Eq. (14). Therefore, the velocity information is ignored in the IPCP detector.

4 DPSS-MMSE estimator

Sampling the noisy received waveform $r(t) = s_3(t) + \nu(t)$ with sampling time T_s, we will obtain L samples where $s_3(t)$ and $\nu(t)$ are assumed uncorrelated. $\nu(t)$ accounts for all interferences, clutters, and thermal noise and hence can be considered as colored and non-Gaussian noise. Taking into consideration that f_0 is the only known a priori

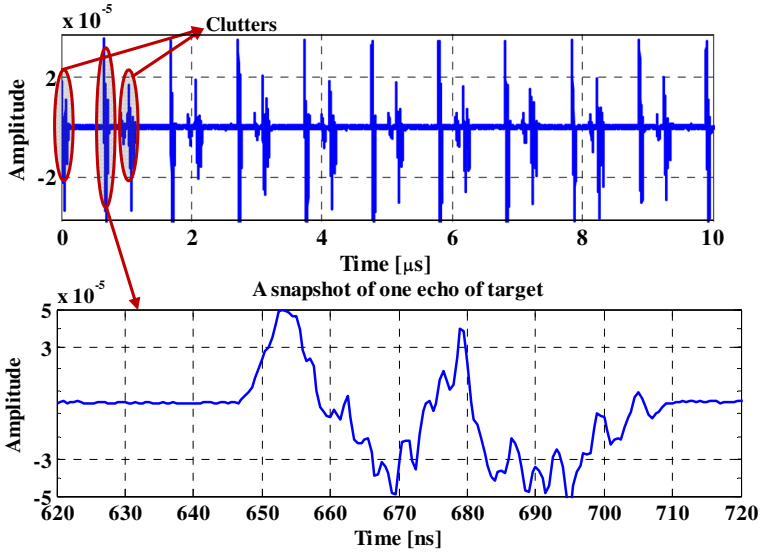

Fig. 3 Backscattered signal from a target. The signal from a target that impinge on the 11-chip barker sequence as the transmitted signal. Chip width is 2 ns and the total pulse width is 22ns. PRI is 1 μs in transmitted signal

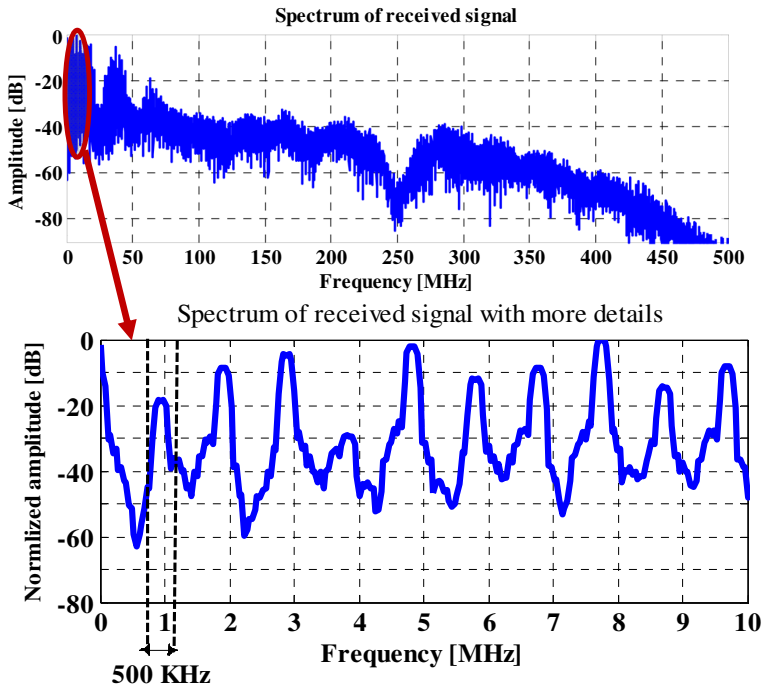

Fig. 4 Spectrum of the backscattered signal from a target. Spectrum of the backscattered signal from a target. The duration of observations in computation of spectrum is 4 PRI s. PRI is 1 μs in the transmitted signal

information, in this section, we will introduce a MMSE estimator for determination of the finite bandwidth signals $a_n(\ell)$, and then, we develop our estimator to detect the presence of the UWB signal and extract the target's range and velocity. In estimating of $a_n(\ell)$, we first expand it by the optimum orthogonal bases. The optimal bases, that is an index-limited sequence with maximum energy concentration in a finite sample interval, is related to the zeroth discrete prolate spheroidal sequence (DPSS) [17]. In accordance with this decomposition, $a_n(\ell)$ can be expressed in terms of DPSS sequences

$$\begin{aligned} a_n(\ell) &= \sum_{m=1}^{\mathcal{M}} c_{mn}\phi_m(\ell) = \Phi(\ell)^T \mathbf{C}_n, \quad \ell = 0, \cdots, L-1 \\ \Phi(\ell) &= [\phi_1(\ell)\ \phi_2(\ell)\ \cdots\ \phi_{\mathcal{M}}(\ell)]^T \\ \mathbf{C}_n &= [c_{1n}\ c_{2n}\ \cdots\ c_{\mathcal{M}n}]^T, \end{aligned} \tag{16}$$

where $\{\phi_m(\ell)\}_{m=1}^{\mathcal{M}}$ are DPSS orthonormal sequences, $\mathbf{C}_n$ is the coefficient vector. $\mathcal{M} < L$ is the order of expansion and depends on the normalized bandwidth of $a_n(t)$, W, and observation length, L,

$$\mathcal{M} = \lceil 2WLT_s \rceil + 1. \tag{17}$$

We use linear estimation model with time-varying weights, which is defined as

$$\hat{a}_n(\ell) = \mathbf{w}_n(\ell)^H \mathbf{r}, \tag{18}$$

where $\mathbf{r}$ is the $L \times 1$ observation vector has been made by sampled received waveform and $\mathbf{w}_n(\ell)$ are time-varying weights. Substituting Eq. (8) in to the sampled received

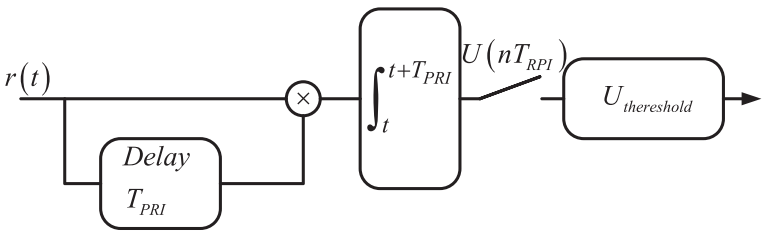

Fig. 5 The block diagram of the IPCP receiver

signal, $r(\ell) = s_3(\ell) + \nu(\ell)$, the matrix presentation of the observation vector $\mathbf{r}$ will be:

$$\mathbf{r} = \sum_{n=-N/2}^{N/2} \mathbf{F}_n \mathbf{C}_n + \upsilon, \tag{19}$$

where υ is the $L \times 1$ noise vector which is uncorrelated to the signal and $\mathbf{F}_n$ is a $L \times \mathcal{M}$ matrix with entries:

$$f_n(i,m) = \left\{ \phi_m(i) e^{j\frac{2\pi n}{T_p} i} \right\}, \begin{cases} 0 \le i \le L-1 \\ 1 \le m \le \mathcal{M} \end{cases} \tag{20}$$

Incorporating Eq. (19) into Eq. (18), the expansion of $\hat{a}_n(\ell)$ is achieved:

$$\begin{aligned} \hat{a}_n(\ell) &= \mathbf{w}_n(\ell)^H \sum_{n'=-N/2}^{N/2} \mathbf{F}_{n'} \mathbf{C}_{n'} + \mathbf{w}_n(l)^H \upsilon \\ &= \mathbf{w}_n(\ell)^H \mathbf{F}_n \mathbf{C}_n + \sum_{n'=-N/2, n' \neq n}^{N/2} \mathbf{w}_n(\ell)^H \mathbf{F}_{n'} \mathbf{C}_{n'} + \mathbf{w}_n(\ell)^H \upsilon. \end{aligned} \tag{21}$$

The above equation reveals that each estimate is formed of two components: the first depends on the time-varying amplitude at the frequency of interest ω_n, while the second is an error term which depends on all the other components of $r(\ell)$ at frequencies separated from ω_n and noise. The optimal estimator must produce the accurate time-varying amplitude from the first component and minimize the contribution of the error term. In other words, we need to impose the restrictions that:

$$\mathbf{w}_n(\ell)^H \mathbf{F}_n = \Phi(\ell)^H. \tag{22}$$

Also, we have to minimize the mean-squared error (MSE):

$$\mathrm{MSE}(\ell) = E\left\{ \left| a_n(\ell) - \hat{a}_n(\ell) \right|^2 \right\}. \tag{23}$$

Minimization of Eq. (23) is performed subject to the constraint (Eq. 22) using the method of Lagrange multipliers, i.e., we have to minimize the cost function:

$$\begin{aligned} J(\ell) = {} & \mathbf{w}_n(\ell)^H \Theta \mathbf{w}_n(\ell) + \mathbf{w}_n(\ell)^H \mathbf{R}_\upsilon \mathbf{w}_n(l) \\ & - \left[\mathbf{w}_n(\ell)^H \mathbf{F}_n - \Phi(\ell)^H \right] \lambda, \end{aligned} \tag{24}$$

where

$$\Theta = \sum_{n'=-N/2, n' \neq n}^{N/2} \mathbf{F}_{n'} E\left\{ \mathbf{C}_{n'} \mathbf{C}_{n'}^H \right\} \mathbf{F}_{n'}^H, \quad \mathbf{R}_\upsilon = E\left\{ \upsilon \upsilon^H \right\} \tag{25}$$

and λ is a $\mathcal{M} \times 1$ vector of Lagrange multipliers. By setting the first derivative of the cost function to zero, we arrive at optimum least square weights as [23]:

$$\mathbf{w}_n(\ell) = \mathbf{F}_n \Phi(\ell). \tag{26}$$

By using this model, MMSE is determined as

$$\mathrm{MMSE}(\ell) = \left(1 + \sigma_\upsilon^2\right) \sum_{m=1}^{\mathcal{M}} |\phi_m(\ell)|^2, \tag{27}$$

where σ_υ^2 is the variance of colored or AWG noise. Although, MMSE seems time-dependent in Eq. (27), but it is almost constant in practice and is $\frac{\mathcal{M}}{L}\left(1 + \sigma_\upsilon^2\right)$. By decreasing $\mathcal{M}$ and increasing L, the MMSE will be decreased. Therefore, the suitable selection of L which depends on the bandwidth of $a_n(t)$ alleviate noise as much as possible. The number of L and $\mathcal{M}$ is set by an educated guesstimate. In the two following sections the extraction of range and velocity of the target from estimated time-varying coefficients have been described.

5 Range processing

In this section, we use energy detector to find the range of the target. We can write the received signal as

$$\begin{aligned} r(t) &= \sum_{n=-N/2}^{N/2} r_{\omega_n}(t) + \upsilon(t) \\ r_{\omega_n}(t) &= a_n(t) e^{j\omega_n t}. \end{aligned} \tag{28}$$

And the energy of the received signal in each time range cell is expressed as

$$\mathcal{E}_k = \int_{(k-1)T_g}^{kT_g} |r(t)|^2 dt, \tag{29}$$

where T_g is the the range cell and $\mathcal{E}_k$ is the energy of the k^{th} range cell. Neglecting the very slight overlap of $r_{\omega_n}(t)$'s, $|r(t)|^2$ can be replaced by:

$$|r(t)|^2 = \sum_{n=-N/2}^{N/2} \left| r_{\omega_n}(t) \right|^2 + |\upsilon(t)|^2. \tag{30}$$

Therefore, the energy of the kth range cell can be expressed as:

$$\begin{aligned} \mathcal{E}_k &\approx \sum_{n=-N/2}^{N/2} \int_{(k-1)T_g}^{kT_g} \left| r_{\omega_n}(t) \right|^2 dt + \varepsilon_k \\ &= \sum_{n=-N/2}^{N/2} \int_{(k-1)T_g}^{kT_g} |a_n(t)|^2 dt + \varepsilon_k, \end{aligned} \tag{31}$$

where ε_k is the energy of noise in the kth range cell. The detection algorithm can be implemented under two hypotheses test:

$$\begin{cases} r(t) = s_3(t) + \upsilon(t) & \mathcal{H}_1 \\ r(t) = \upsilon(t) & \mathcal{H}_0, \end{cases}$$

where $\mathcal{H}_1$ shows the presence of the target and $\mathcal{H}_0$ shows the absence of the target. By considering estimated energy in every range cell as decision statistics and based on

Eq. (31), the decision statistics can be presented as the combination of the energy of estimated coefficients:

$$l(\mathbf{a}) = \frac{1}{NL} \sum_{n=-N/2}^{N/2} \sum_{i \in \mathcal{A}^k} \left| \hat{a}_n(i) \right|^2, \tag{32}$$

where $l(\mathbf{a})$ is the decision statistics and $\mathcal{A}^k$ is a countable set of the length of $L = \left\lfloor \frac{T_g}{T_s} \right\rfloor$,

$$\mathcal{A}^k \triangleq \{ i \in \mathbb{Z} \ : \ (k-1)L, \ldots, kL-1 \}. \tag{33}$$

Therefore, the decision rule can be given by

$$l(\mathbf{a}) \underset{\mathcal{H}_0}{\overset{\mathcal{H}_1}{\gtrless}} \gamma, \tag{34}$$

where γ is threshold. To define the threshold for a given the probability of false alarm (P_{FA}), we have to determine an analytical expression for the distribution function of $l(\mathbf{a})$ under $\mathcal{H}_0$. This distribution function is approximated as a Gaussian distribution:

$$l(\mathbf{a}) \sim \mathcal{N}\left(\mu, \Sigma^2\right), \tag{35}$$

where μ and Σ^2 are mean and variance, respectively. In this approximation, considering large number of elements in observation vector $\mathbf{r}$, central limit theorem is used. When the amount of L is large enough, the approximation of distribution of $l(\mathbf{a})$ under $\mathcal{H}_0$ as a Gaussian is independent of the type of noise (AWGN, colored or non-Gaussian). In Section 7 the Kolmogorov-Smirnov test is used to experimentally show the conformity of this approximation. The statistical average in Eq. (35) for the most general case, where no statistical assumption on the distribution of noise is required, is expressed as:

$$\mu = \frac{1}{NL} \sum_{n=-N/2}^{N/2} \sum_{i=0}^{L-1} \mathbf{w}_n^H(l) \, \mathbf{R}_\upsilon \mathbf{w}_n(l). \tag{36}$$

In this case, variance cannot be evaluated in closed form. But, for *iid* noise, Eq. (36) can be simplified, hence, we are able to evaluate statistical average and variance in closed form as the following:

$$\mu = \frac{\sigma_\upsilon^2}{L} \sum_{i=1}^{L} \sum_{m=1}^{M} |\phi_m(i)|^2, \quad \Sigma = \sqrt{\frac{2\sigma_\upsilon^4}{L} \sum_{i=1}^{L} \left(\sum_{m=1}^{M} |\phi_m(i)|^2 \right)^2}. \tag{37}$$

This allows the probability of false alarm, P_{FA} to be approximated as

$$P_{FA} = P\left(l(\mathbf{a}) | \mathcal{H}_0\right) = Q\left(\frac{\gamma - \mu}{\Sigma}\right), \tag{38}$$

where $Q(\cdot)$ is the tail probability function of a zero-mean unit-variance Gaussian random variable. Therefore, for a the given probability of false alarm, we are able to determine the threshold.

The probability of false alarm is decreased, and simultaneously, the probability of detection is increased by increasing the length of L or equivalently the time range cell T_g. We note that $1/T_g$ is the range resolution and it cannot be a large number. The appropriate value for T_g for the purpose of target range detection is the reciprocal of the received signal bandwidth. But, it can be set smaller amount when more range resolution is needed. the amount of this parameter is depend on the scenario of detection.

6 Velocity processing

As previously mentioned in Section 2.3, $a_n(t)$ is a band-limited signal around the Doppler frequency, so the peak of $S_a^{nn}(t;f)$ can determine the Doppler frequency and the velocity of the target can henceforth be determined. Based on Wiener-Kintchin theorem

$$S_a^{nn}(t;f) = \int_{-\infty}^{\infty} R_a^{nn}(t;\tau) \, e^{j2\pi f \tau} d\tau. \tag{39}$$

Again, based on Eq. (51) we have

$$S_a^{nn}(t;f) = KP^2 |c_n|^2 S_g^{nn}(t; f - F_d). \tag{40}$$

As the Doppler frequency is independent of time, the peak of Eq. (40) when time-averaged, will define the Doppler frequency.

$$\begin{aligned} \overline{S_a^{nn}(f)} &= \lim_{T \to \infty} \frac{1}{T} \int_{-T/2}^{T/2} S_a^{nn}(t,f) \, dt \\ &= KP^2 |c_n|^2 \overline{S_g^{nn}(f - F_d)}. \end{aligned} \tag{41}$$

Based on [24], the time-averaged signal in Eq. (41) can be considered as a spectral correlation density function

at zero cycle frequency whose consistent estimator is the frequency-smoothed cyclic periodogram [24]

$$S_a^{nn}(t,f) = \lim_{T\to\infty}\lim_{\Delta f\to 0}\frac{1}{T}\int_{f-\Delta f/2}^{f+\Delta f/2}\frac{1}{\Delta f}\left|A_T^n(t,\lambda)\right|^2 d\lambda, \tag{42}$$

where

$$A_T^n(t,\lambda) = \int_{t-T/2}^{t+T/2} a_n(s)\, e^{-j2\pi\lambda s} ds. \tag{43}$$

In addition, we define $\mathcal{P}$ as

$$\sqrt{T\Delta f}\left(\widehat{S_a^{nn}(t,f)} - \overline{S_a^{nn}(f)}\right). \tag{44}$$

In [24], it has been shown that $\mathcal{P}$ is an asymptotically zero-mean complex Gaussian random variable with $\sigma_{\mathcal{P}} = 1$.

To compute $A_T^n(t,\lambda)$, $a_n(iT_{PRI})$, the samples of $a_n(t)$ at sampling time iT_{PRI}, are to be used as the inputs for discrete version of Eq. (43) which it is FFT processing. The resolution of the frequency must be selected such that $\Delta f \geq 1/T$ (in our scenario T is equal coherent processing interval T_CPI). So the best resolution for the Doppler frequency can be $1/T$ which, based on Eq. (44), causes maximum variance of the error in the estimation. To reduce the variance of the error we have to increase Δf. By incoherent summation of $S_a^{nn}(t;f)$ over all harmonies we are able to improve the signal-to-noise ratio in the estimation. After this is done, the energy detection could be employed to detect the Doppler frequency. Since, $S_a^{nn}(t;f)$ has been modulated from nf_0 to the baseband, we shall use $S_a^{nn}(t;f-nf_0)$ instead of $S_a^{nn}(t;f)$ in the incoherent summation. Therefore, the result of incoherent summation can be expressed as:

$$S_r(t;f) = \sum_{n=-N/2}^{N/2} S_a^{nn}(t;f-nf_0) \tag{45}$$

and

$$\overline{S_r(f)} = \sum_{n=-N/2}^{N/2} \overline{S_a^{nn}(f-nf_0)}. \tag{46}$$

The estimator $\sqrt{T\Delta f}\widehat{S_r(t,f)}$ which is an asymptotically complex normal random variable with the mean of $\sqrt{T\Delta f}S_r(f)$ can be computed based on Eq. (42). Based on energy detection, the decision statistics under two hypotheses can be represented as $l(\mathbf{a}) = T\Delta f|\widehat{S_r(t,f)}|^2$.

For white noise assumption under $\mathcal{H}_0$, the mean of the estimator is expressed as:

$$\sqrt{T\Delta f}\ \overline{S_r(f)} = \sqrt{T\Delta f}\sigma_v^2.$$

Therefore, the random variable $l(\mathbf{a})$ has the non-central chi-square distribution, expressed as:

$$f(l(\mathbf{a})|\mathcal{H}_0) = \frac{1}{2}e^{-\left(\frac{l(\mathbf{a})+\lambda}{2}\right)} I_0\left(\sqrt{\lambda l(\mathbf{a})}\right), \tag{47}$$

where $\lambda = T\Delta f\sigma_v^4$ and $I_0(\cdot)$ is the zeroth order modified Bessel function of the first kind. The probability of false alarm for the threshold γ, hence, is expressed as:

$$P_{FA} = P(l(\mathbf{a}) \geq \gamma|\mathcal{H}_0) = Q_1\left(\sqrt{\lambda}, \sqrt{\gamma}\right), \tag{48}$$

where $Q_1(.,.)$ is the Marcum Q-function. Again, to decrease the probability of false alarm and to increase the probability of detection simultaneously, Δf should be increased. Increasing Δf would also cause the velocity resolution to increase. Here, it should be taken into account that variations of the Doppler frequency lower than Δf cannot be sensed. As a result, in high-resolution velocity applications, the FFT processing time i.e., T, must be large enough. Since in our novel detection, the spectrum of signal is determined by a non-stationary analysis (Eq. 42), it is still valid for large T.

7 Simulation and results

Computer simulations and an experimental test are carried out to illustrate the performance of the proposed algorithm. In the experimental test, we have produced an ultra-short pulse signal with features mentioned in Table 1 by a signal generator excited with an impulse generator. The generated signal after near 13dB amplification is inputted to a horn antenna with an approximately 10° beamwidth in both elevation and azimuth. Next, the signal is impinged upon the "remote control Skyartec mini Cessna" plain flying at the distance range of 90 to 130 m. The backscattered signal after being received by the antenna and passing through the circulator will be caught by a fast oscilloscope. A fast switch is used to alleviate ground clutter and to protect the oscilloscope. The output signal of the oscilloscope is logged by a computer at three positions of the target mentioned in the Table 2. Since we have not used array antenna in our experimental test, the received signal model, previously mentioned in Section 2, will be valid for $P = 1$ (P is the number of radiators in the array antenna depicted in Fig. 2). The experimental setup is shown in Fig. 6.

Since the target in the test is near the radar, the received signal level is high. Actually, by measuring the noise and signal level at the input of the oscilloscope we find that the SNR is around 26 to 30dB in various range mentioned in Table 2. To produce multi-target scenarios, we consider this signal as the noiseless signal and combine them to produce a signal refrying to three targets in three position mentioned in Table 2. To produce (non)-Gaussian white (colored) noisy signal, we make the signal under the test by adding noise to the noiseless signal. The colored noise

Table 1 Features of transmitted signal and receiver

Parameter	Info	Parameter	Info
T_{PRI}	1 μs	L	8000
Carrier frequency	3 GHz	CPI	7 ms
Pulse width	2 ns	Bandwidth	500MHz
T_{obs}	4 μs	Velocity resolution	7 m/s
N	40	Range resolution	$>$ 1 m
$\mathcal{M}$	5	Max of range	150 m

is constructed by passing AWGN noise over a low-pass FIR filter. The order of this filter is 9 and its bandwidth is 10MHz. The non-Gaussian noise used in this paper is the Middleton Class-A noise. From [25, 26] the probability of density function for the Class-A noise process is considered as:

$$f_x(x) = e^{-A} \sum_{m=0}^{\infty} \frac{A^m}{m!\sqrt{2\pi\sigma_m^2}} e^{-\frac{x^2}{2\sigma_m^2}},$$

where

$$\sigma_m^2 = \frac{m/A + \Gamma}{1+\Gamma}.$$

According to this pdf, this noise is thereby a weighted sum of Gaussian distributions. σ_m^2 is the variance of the mth Gaussian distribution. A, which is called impulsive index [25] is set to one in this paper. Γ refers to the portion of the power of each Gaussian part in the total distribution which is set to $\Gamma = 0.01$ in this paper. In this paper, we consider $m = 2$.

In this paper, to drive an equation between false alarm rate and the threshold, i.e., Eq. (35), the hypothesis statistic $l(\mathbf{a})$ is approximated as Gaussian random variable. In this section, the conformity of this approximation is experimentally proved at the first. Based on Eq. (18), $\hat{a}_n(i)$ is a weighted combination of elements of $\mathbf{r}$. Since the length of $\mathbf{r}$, i.e., L, is large, according to central limited theorem $\hat{a}_n(i)$ has the Gaussian distribution. The amount of $L = 8000$ is large enough that the Gaussian distribution is independent of the type of noise (AWGN, colored or non-Gaussian). The Kolmogorov-Smirnov test, is a very common and powerful test in comparing the values in the given data vector, such as $\hat{a}_n(i)$, to Gaussian distribution [28]. We use this test for 100 samples of $\hat{a}_n(i)$ in the significance level 15 % (this parameter mentions to the error of unconformity [28]). The test approves the conformity in all types of noise. Therefore, There is no assumption on noise. Since, $\hat{a}_n(i)$ have almost standard normal distribution, $l(\mathbf{a})$ has the chi-squared distribution with N degrees of freedom. The N is large enough to let us approximate the chi-squared distribution with Gaussian distribution. Again, the Kolmogorov-Smirnov test is done for 100 samples of $l(\mathbf{a})$ in the significance level 15 % and the conformity is approved.

Table 2 Targets information

	Velocity	Range
Target #1	+15 m/s^a	70 m
Target #2	-20 m/s	95 m
Target #3	-35 m/s	115 m

[a]plus for close to the radar, and minus for far from the radar

In all simulation in this paper, the SNR is considered as the power of the noiseless signal over the power of noise that is added to the noiseless signal. In the first simulation, we have assumed three scenarios with three targets mentioned in Table 2. The noise is assumed to be AWGN for the first, colored Gaussian for the second and non-Gaussian white for the third scenario.

Range and velocity detection are done for each case. Since, the decision statistics and the threshold in dimension of range and velocity are completely different jointly detection is impossible. The detection procedure is done for both range and velocity separately. In the simulations in every hypotheses testing procedure, a target detection is considered as a correct detection if the detection of both range and velocity are correct. Also, in the simulations, a false alarm is considered if a false alarm detection happens in range or velocity and a miss detection is considered if a target is missed in range or in velocity. The hypotheses testing procedure is performed in every cell. In general scenarios in the application considered in this simulation and experimental results, the length of the target is more than one meter in its dimension with maximum length and the distance between two targets can not be less than three meters. Since, the maximum length of target is more than one meter, in the detection algorithm we use the time of range cell, $T_g = 10$ ns, that causes 1.5 m range resolution. Also, we consider 5 ns for time of overlap in the cells. Since, the distance between two targets is not less than three meters, in the implementation of detection algorithm, when the energy of three adjacent cells or two adjacent cells or one cell pass the threshold, we consider it as a one target.

The range-velocity plot for SNR = 2 dB is shown in Fig. 7a. The range and velocity views are shown in Fig. 7b, c, respectively. The energy of the cell for each range cell is computed in range domain, and $\widehat{S_r(t;f)}$ is computed in a CPI time and time is averaged out in velocity domain. In Fig. 7a, peaks which can be seen in

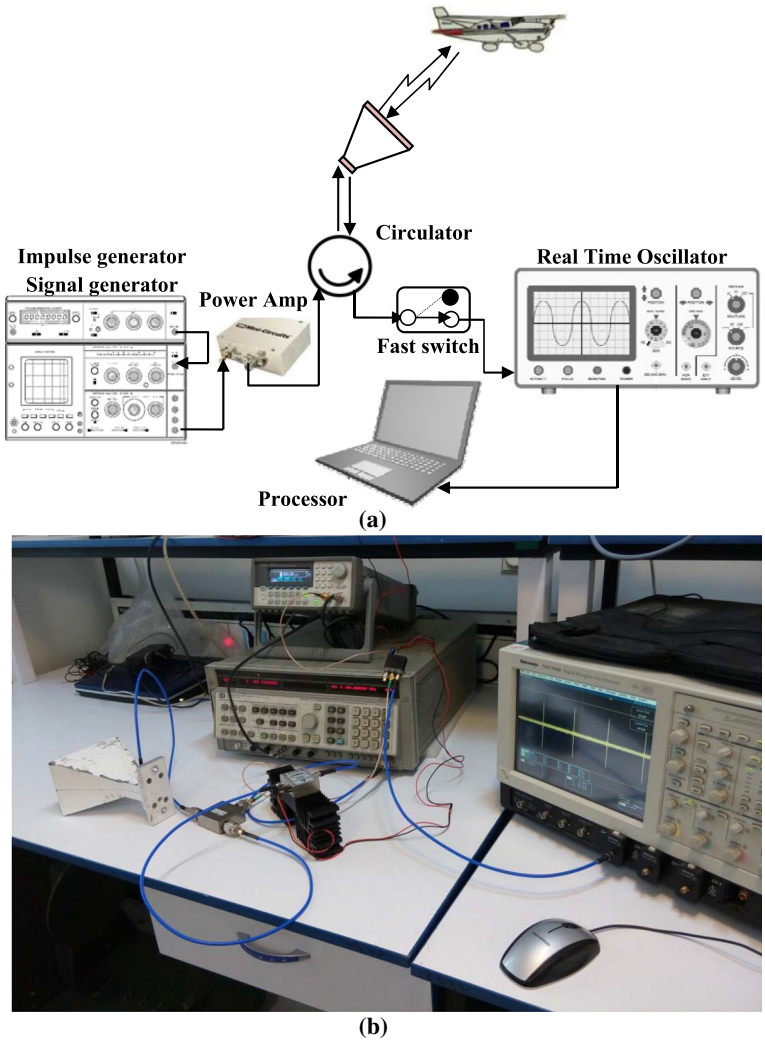

Fig. 6 The Experimental setup. **a** Schematic **b** Setup in the laboratory

the zero velocity are related to non-stationary clutters. In this figure, the robustness of the purposed algorithm in presence of the non-Gaussian and colored noise can be clearly perceived. In Fig. 7b, the peaks of energy happen just in the place of velocity of targets. These peaks, happening in all three noise scenario, are good references for the ability of proposed detection in extraction of velocity.

The time-varying spectrum $\widehat{S_r\left(t;f\right)}$ for the target at the velocity of -37 m/s, referring to -744 Hz, is depicted in Fig. 8 as an example of time-varying spectrum. This figure is to provide an evidence that time-varying coefficients have finite band width around Doppler frequency. It is seen that the bandwith of signal is around 350 Hz.

The new detector is compared to the IPCP in two next simulations. In these simulations, the performance of novel detector is surveyed in a single target as well as three targets in the presence of (non)-Gaussian white (colored) noise. on the other hand, IPCP detector is used only for single target detection in the presence of white Gaussian noise. In the first simulation, the priority of proposed detector is shown by ROC plot for $SNR = 2$ dB in Fig. 9. In this figure, it is seen the superiority of the proposed detector over IPCP in both single and three targets in the presence of AWGN. The probability of detection in the proposed detector in single target is around 0.11 better than IPCP in false alarm rate 10^{-2}. This amount is 0.09 in three targets case. Assuming the probability of detection 0.85 as the applicable performance, it can be seen that the proposed detector is a applicable in all scenarios for noise, when false alarm rate is around 0.06 and $SNR = 2$ dB. In the second simulation (Fig. 10), the probability of detection for various SNR in $P_{fa} = 10^{-2}$ has been regarded. According to this figure, the prob-

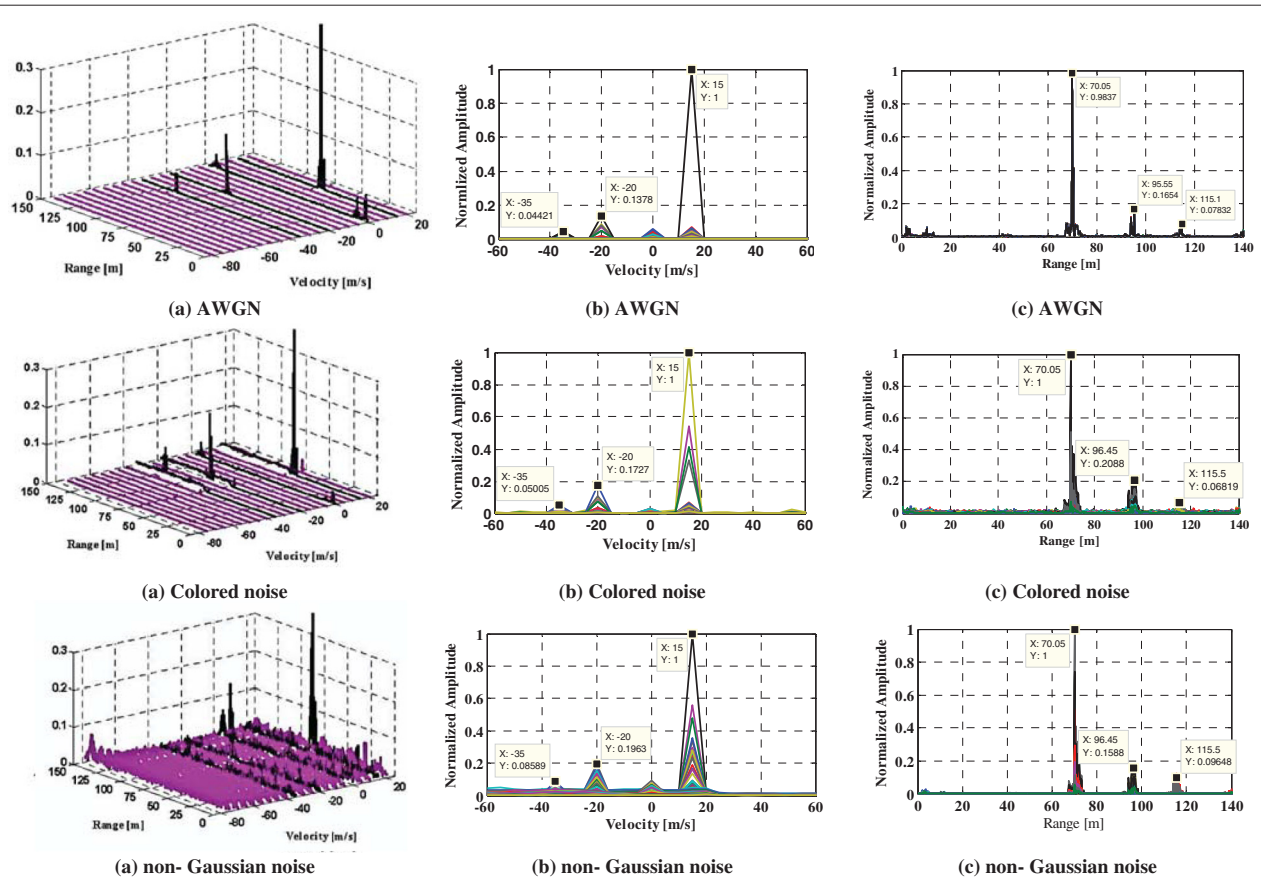

Fig. 7 Range-velocity plot. This plot depicts range-velocity plot for three targets in SNR = 2 dB when noise is AWGN, Gaussian-colored and non-Gaussian white. Energy of the cell for each range cell is computed in range domain, $\widehat{S_r(t;f)}$ is computed in a CPI time and time is averaged out in velocity domain. **a** Range-velocity plot. **b** Velocity view. **c** Range view

ability of detection 0.9 is achieved in the $SNR = -2$ dB in single target detection and $SNR = -0.5$ dB in three targets detection. This performance is achieved in IPCP in $SNR = 3.2$ dB which is around 5.2 dB worse than the performance of novel detector for single target detection and 3.7 dB worse than for three targets detection. Assuming the probability of detection 0.85 as the applicable performance, it is seen that in $SNR = 5$ dB the novel detector is applicable in all scenarios for noise.

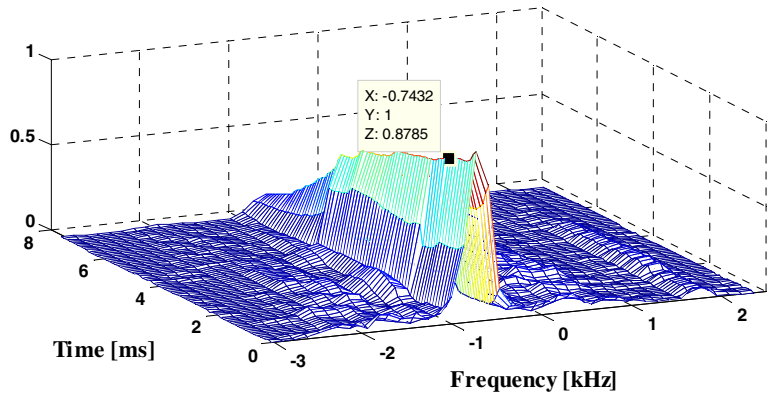

Fig. 8 $\widehat{S_r(t;f)}$ for the target. the velocity of target is −37 m/s. It can be seen that $S_r(t;f)$ is band-limited around Doppler frequency

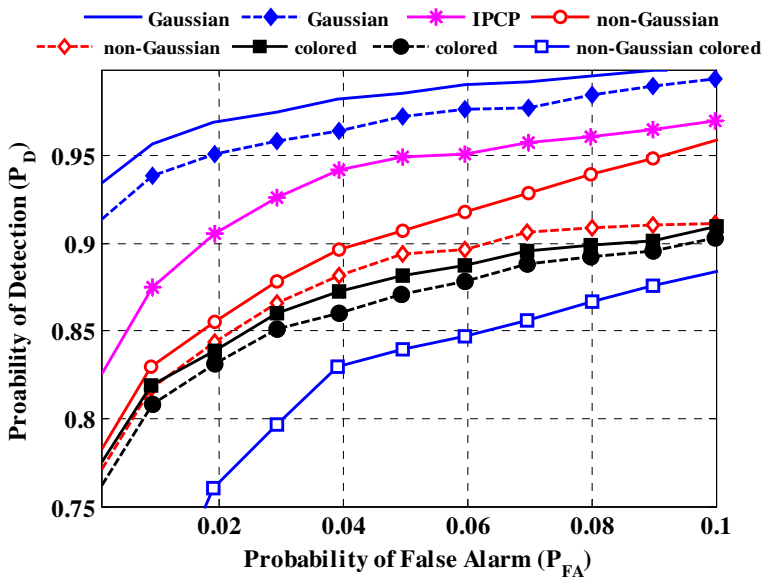

Fig. 9 Receiver operation characteristics (ROC). In this plot SNR = 2 dB. *Solid line* shows ROC for single target and *dashed line* shows ROC for three targets

8 Conclusion

In this paper, we have demonstrated that the receivers in ultra-wideband impulse radar based on IPCP use the received signal as the reference in their correlator which leads to remove Doppler frequency. Also, the Fourier series model with time-varying coefficients is perceived as a convenient model for non-stationary received signal in UWB impulse radar. Accordingly, the innovative MMSE estimator is introduced to evaluate the coefficients. Utilization of the time-varying weights in the estimator makes the blind noise-suppression from non-stationary signals without correlation, conceivable. The robust detection is proposed to extract the range and velocity in accordance with the estimator. Versatile results in comparison to IPCP and robustness to the alteration of noise features do verify the ability of our novel detector to be used in future applications.

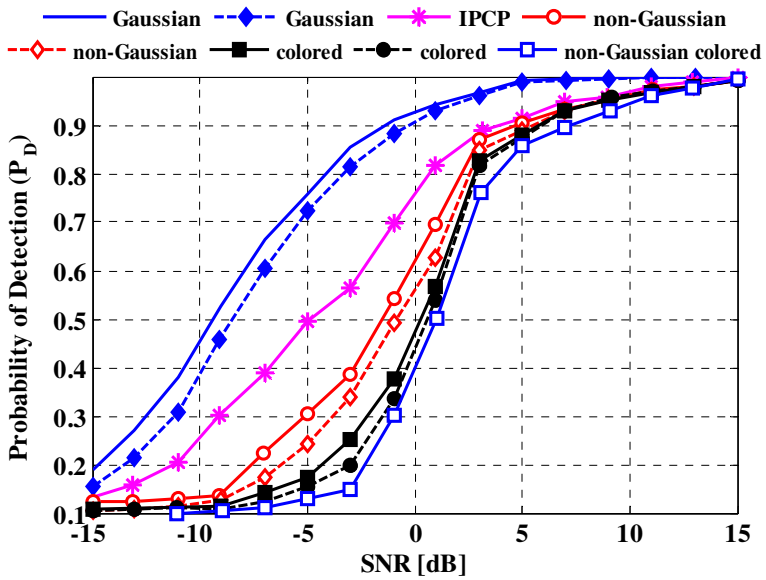

Fig. 10 Probability of detection versus SNR in $P_{fa} = 10^{-2}$. *Solid line* for single target and *dashed line* for three targets

9 Appendix A: Autocorrelation of time-varying coefficients

In this section, we have computed the correlation function and the spectrum of the time-varying coefficients $a_n(t)$

$$\begin{aligned} R_a^{n_1 n_2}(t;\tau) &= E\left\{a_{n_1}(t)\, a_{n_2}^*(t+\tau)\right\} \\ &= P^2 c_{n1} c_{n2}^* e^{-j2\pi F_d \tau} \sum_{m=1}^{M}\sum_{k=1}^{K}\sum_{\hat{m}=1}^{M}\sum_{\hat{k}=1}^{K} E\Big\{ g_{mn_1}(t)\, g_{\hat{m}n_2}^*(t+\tau) \\ &\quad e^{j\left(\varphi_k+\phi_m+\theta_{n_1 km}\right)} e^{-j\left(\varphi_{\hat{k}}+\phi_{\hat{m}}+\theta_{n_2\hat{k}\hat{m}}\right)} \Big\}, \end{aligned} \tag{49}$$

where

$$g_{mn} = \alpha_{mn}(t)\, e^{-j2\pi f_c(2\kappa_m(t))}.$$

Since, we do not have any information about ε_k and δ_m, we can suppose uniform distribution in $[-L_r/2c \;\; L_r/2c]$ and $[-L_t/2c \;\; L_t/2c]$ for ε_k and δ_m, respectively. This assumption would cause uniform distribution in $[-\pi, \pi]$ for $U_k = 2\pi f_c \varepsilon_k$ and $V_m = 2\pi f_c \delta_m$. By this, for $k \neq \hat{k}$ and $m \neq \hat{m}$ the expectation in Eq. (49) can be written as

$$\begin{aligned} &E\left\{ g_{mn_1}(t)\, g_{\hat{m}n_2}^*(t+\tau) e^{j\left(\varphi_k+\phi_m+\theta_{n_1 km}\right)} e^{-j\left(\varphi_{\hat{k}}+\phi_{\hat{m}}+\theta_{n_2\hat{k}\hat{m}}\right)} \right\} \\ &= \frac{1}{(2\pi)^4} \int_{2\pi}\int_{2\pi}\int_{2\pi}\int_{2\pi} E\left\{ g_{mn_1}(t)\, g_{\hat{m}n_2}^*(t+\tau)\, e^{j\left(\theta_{n_1 km}-\theta_{n_2\hat{k}\hat{m}}\right)} \right\} \\ &e^{j\left(U_k - U_{\hat{k}} - V_m - V_{\hat{m}}\right)} dU_k dU_{\hat{k}} dV_m dV_{\hat{m}} = \\ &E\left\{ g_{mn_1}(t)\, g_{\hat{m}n_2}^*(t+\tau)\, e^{j\left(\theta_{n_1 km}-\theta_{n_2\hat{k}\hat{m}}\right)} \right\} \delta\left(k-\hat{k}\right) \delta\left(m-\hat{m}\right). \end{aligned} \tag{50}$$

For $k = \hat{k}$ and $m = \hat{m}$ the correlation function can be expressed as

$$\begin{aligned} &R_a^{n_1 n_2}(t;\tau) = \\ &P^2 c_{n1} c_{n2}^* e^{-j2\pi F_d \tau} \sum_{m=1}^{M}\sum_{k=1}^{K} E\left\{ g_{mn_1}(t)\, g_{mn_2}^*(t+\tau) \right\} \\ &\frac{2c}{L_r}\frac{2c}{L_t} e^{j(\omega_{n_1}-\omega_{n_2})\left(\frac{d\cos(\phi)-2R}{c}\right)} \\ &\int_{-L_t/2c}^{L_t/2c}\int_{-L_r/2c}^{L_r/2c} e^{j(\omega_{n_1}-\omega_{n_2})(\varepsilon_k - 2\delta_m)} d\varepsilon_k d\delta_m \\ &= KP^2 c_{n1} c_{n2}^* e^{-j2\pi F_d \tau} \frac{\sin(\upsilon_r)}{\upsilon_r} \frac{\sin(\upsilon_t)}{\upsilon_t} R_g^{n_1 n_2}(t;\tau), \end{aligned} \tag{51}$$

where $\upsilon_r = \left(\omega_{n_1} - \omega_{n_2}\right) L_r/2c$, $\upsilon_t = \left(\omega_{n_1} - \omega_{n_2}\right) L_t/2c$ and

$$R_g^{n_1 n_2}(t;\tau) = \sum_{m=1}^{M} E\left\{ g_{mn_1}(t)\, g_{mn_2}^*(t+\tau) \right\}. \tag{52}$$

Let us consider $g_{mn}(t) = b_n g_m(t)$, where b_n are samples of frequency response of the targets and strongly depend on shape and material of the target. Therefore, we have $R_g^{n_1 n_2}(t;\tau) = b_{n_1} b_{n_2}^* R_g(t;\tau)$. In [27], for a typical example, it has been proved that $g_m(t)$ is a band-limited process for long time observations and its bandwidth mostly depends on the rotational speed around the axis which is orthogonal to the plane containing L_t, and also on the bandwidth of transmitted signal.

Competing interests
The authors declare that they have no competing interests.

Author details
[1] Amirkabir University of Technology, Tehran, Iran. [2] University of Washington, Seattle, WA, USA.

Received: 26 June 2015 Accepted: 18 April 2016
Published online: 14 May 2016

References

1. RJ Fontana, Recent system applications of short-pulse ultra-wideband (UWB) technology. IEEE Trans. Microwave Theory Tech. **52**(9), 2087–2104 (2004)
2. IY Immoreev, Practical applications of UWB technology. IEEE Tran. AES. **25**(2), 36–42 (2010)
3. GM Hussain Malek, Ultra wideband impulse radar, An overwiev of the principles. IEEE AES. Mag. **52**(9), 9–14 (1998)
4. J Hu, G Zhu, T Jin, et al, Adaptive through-wall indication of human target with different motions. IEEE Geosci. Remote Sensing Lett. **11**(5), 911–915 (2014)
5. W Guohua, Z Yuxiang, W Siliang, in *Proc. IEEE Int. Conf. Radar*. Detection and localization of high speed moving targets using a short-range UWB impulse radar, (2008)
6. JD Taylor, *Ultra-wideband radar technology. Chapter 10*. (CRC Press, 2001)
7. IY Immoreev, Ultra wideband radars: futures and capabilities. J. Commun. Technol. Electron. **54**(1), 1–26 (2009)
8. IY Immoreev, in *Proc. IEEE Int. Conf. Ultra-Wideband*. Detection of UWB signals reflected from complex targets, (2002)
9. AG Yarovoy, LP Ligthart, J Matuzas, et al, UWB radar for human Benng detection. IEEE AES. Mag. **21**(3), 10–14 (2006)
10. S Singh, Q Liang, et al, Sense through wall human detection using UWB radar. EURASIP J. Wireless Commun. Netw. **2011**(1), 1–11 (2011)
11. Y Xu, S Wu, et al, A novel method for automatic detection of trapped victims by ultrawideband radar. IEEE Trans. Geosci. Remote Sensing. **50**(8), 3132–3142 (2012)
12. JH Lee, MH Jang, S Ko, in *Proc. Eur. Radar Conf*. Measuring the target range and relative velocity in UWB radar for automobile applications, (2011)
13. B Sobhani, E Paolini, A Giorgetti, et al, Target tracking for UWB multistatic radar sensor networks. IEEE J. Sel. Topics Signal Process. **8**(1), 125–136 (2014)
14. B Sobhani, M Mazzotti, et al, in *Proc. IEEE ICUWB*. Multiple target detection and localization in UWB multistatic radars, (2014)
15. GS Gill, in *IEEE Trans. Electromagn. Compat.* Ultra-wideband radar using Fourier synthesized waveforms, vol. 39.2, (1997), pp. 124–131
16. AT Hosseini, H Amindavar, in *Proc. IEEE CIE Int. Conf. on radar*. Cyclostationary detector in ultra Wideband Impulse Radar, (2011)
17. DV De Ville, W Philips, I Lemahieu, On the n-dimensional extension of the discrete prolate spheroidal window. IEEE Signal Process. Lett. **9**(3), 89–91 (2002)

18. RJ Baker, BP Johnson, Applying the Marx bank circuit configuration to power MOSFETs. Electron. Lett. **29**(1), 56 (1993)
19. M Niedzwiecki, *Identification of Time-Varying Processes*. (Wiley, New York, 2000)
20. A Berlinet, C Thomas-Agnan, *Reproducing Kernel Hilbert Spaces in Probability and Statistics*. (Kluwer Academic, Boston, 2004)
21. D Slepian, Prolate spheroidal wave functions, Fourier analysis, and uncertainty–V: the discrete case. Bell Syst. Tech. J. **57**(5), 1371–1430 (1978)
22. HJ Landau, HO Pollak, Prolate spheroidal wave functions, Fourier analysis, and uncertainty–III: the dimension of the space of essentially time-limited and band-limited signals. Bell Syst. Tech. J. **41**(4), 1295-1336 (1962)
23. SM Hosseini, H Amindavar, et al, in *IEEE Int. Workshop on SPAWC*. A New Cyclostationary spectrum sensing approach in cognitive Radio, (2010)
24. WA Gardner, A Napolitano, L Paura, Cyclostationarity: Half a century of research. Eles. J. Signal Proccess. **86**(4), 639–697 (2006)
25. D Middleton, Non-gaussian noise models in signal processing for telecommunications: new methods and results for class a and class b noise models. IEEE Tran. on Infor. Theo. **45**(4), 1129–1149 (1999)
26. RB Ash, C Doleans-Dade, *Probability and measure theory*. (2, ed.) (Academic Press, 2000)
27. BH Borden, ML Mumford, A statistical glint/radar cross section target model. IEEE Tran. AES. **19**(15), 781–785 (1983)
28. FJ Massey, The Kolmogorov-Smirnov test for goodness of fit. J. Am. Stat. Assoc. **46**(253), 68–78 (1951)